

1 **Atmospheric small-scale turbulence from**  
2 **three-dimensional hot-film data**

3 **Livia S. Freire · Marcelo Chamecki ·**  
4 **Edward G. Patton**

5  
6 Received: DD Month YEAR / Accepted: DD Month YEAR

7 **Abstract**

8 The behavior of small-scale atmospheric turbulence is investigated using the  
9 three-dimensional Canopy Horizontal Array Turbulence Study (CHATS) hot-  
10 film data. The analysis relies on an *in situ* calibration versus simultaneous  
11 sonic anemometer measurements. The calibration is based on King's law and  
12 geometric relationships between the individual hot-film sensors, and is able  
13 to account for the errors associated with sensors' misalignment and the high  
14 turbulence intensity. The details of the calibration are provided, and its per-  
15 formance is validated by comparing results of spectra and structure functions  
16 with standard wind-tunnel data and model spectra. A single 3h block of data  
17 was selected, containing 33 subblocks of 2 min data without error gaps, whose  
18 statistics were averaged to provide smooth results. These data were measured  
19 above canopy under stable conditions, and correspond to a Taylor Reynolds  
20 number  $Re_\lambda \approx 1550$ . The agreement with wind tunnel results for a similar  
21  $Re_\lambda$  and with model predictions provides a validation for the *in situ* cali-  
22 bration method applied. Furthermore, the results indicate a presence of the  
23 bottleneck effect in the lateral and vertical spectra, in addition to a lack of  
24 inertial range in the second-order structure function due to the low Reynolds  
25 number. An additional analysis of the effect of Reynolds number on the inertial  
26 range is provided using atmospheric data from the literature.

27 **Keywords** Hot-film · Small-scale turbulence · Sonic anemometer · Spectra ·  
28 Structure function

29  

---

Livia S. Freire  
University of São Paulo, São Carlos, SP, Brazil  
E-mail: liviafreire@usp.br

Marcelo Chamecki  
University of California, Los Angeles, CA, USA

Edward G. Patton  
National Center for Atmospheric Research, Boulder, Colorado, USA

## 1 Introduction

Field measurements correspond to one of the main tools used in the understanding and characterization of atmospheric turbulence. For the wind velocity, the vast majority of these measurements is performed by sonic anemometers, which are robust and resistant instruments developed to function across different weather conditions. Sonic anemometers provide the three velocity components, in addition to virtual temperature, by measuring the time taken by sound waves to travel along each of three acoustic paths (Horst and Oncley 2006). These instruments do not require frequent recalibration, but they are limited by the path length between the transducers, which is typically in the order of 0.1 m. As a consequence, turbulent fluctuations with spatial scales smaller than the path length are not captured. In most applications, the scales not captured by the sensor include part of the inertial range and the dissipative scales of the atmospheric flow. Furthermore, the supporting structure of the sensor can also cause flow distortion (Kaimal and Finnigan 1994). Therefore, many turbulence phenomena related to the smallest scales of the flow – including the direct estimation of the turbulent kinetic energy (TKE) dissipation rate itself – cannot be investigated using typical field experiment data.

Differently from field measurements, laboratory experiments of turbulent flows usually rely on hot-film or hot-wire anemometers, also known as constant temperature anemometers (CTA), which are very fine sensors that are able to measure small-scale velocity fluctuations at high frequencies. CTA anemometry is based on the concept of variation of the electrical resistance with temperature, through the use of a heated wire (or film) that senses the changes in heat transfer caused by fluctuations in the fluid velocity. The difference between wire and film is the material composition and diameter (wires are usually one order of magnitude thinner), being recommended for different applications depending on the desired frequency response and resistance (Jørgensen 2005). For atmospheric flows, hot-films are recommended due to their increased strength and stability of calibration, despite the lower frequency response compared to hot-wires (Hasse and Dunckel 1980). CTAs are available in one or multiple sensors per probe, and the output of the sensor is one or multiple time series of voltage that can be directly related to the time series of velocity fluctuations through the use of a calibration curve. One requirement for this method, however, is that the temperature, pressure and composition of the fluid be constant, making the fluid velocity the only variable affecting the heat transfer (Lekakis 1996). Although these conditions can be controlled in the laboratory, they are rarely met in the outdoor environment where atmospheric measurements are performed. The constant calibration required to adjust to changes in air temperature and water vapor mixing ratios make the use of hot-films in atmospheric experiments much less practical.

The most common approach when using hot-film for atmospheric measurements is to perform calibration of each sensor prior to (and sometimes after) the experiment. This can be done in the laboratory or at the experiment site,

75 using a calibration facility or chamber to record the relationship between volt-  
76 age outputs and known velocities. Laboratory calibration of triple hot-films  
77 were used by Miller et al. (1989) in canopy measurements and by Skelly et al.  
78 (2002) in the CASES-99 experiment. Calibrations at the experiment site were  
79 employed for the 31 single probes in the SLTEST facility of the the Great Salt  
80 Lake Desert, USA (Metzger et al. 2007), and by Gulitski et al. (2007) in a  
81 flat grassland region near Pardes-Hanna, Israel, where a multi-wire probe was  
82 used (20 hot wires plus 5 cold wires for temperature measurements, providing  
83 the three velocity components plus temperature, in addition to their spatial  
84 and temporal derivatives).

85 Given the difficulties of frequent and onerous recalibration of the sensor,  
86 the idea of calibrating hot-films after the field experiment using the veloc-  
87 ity data simultaneously measured by a sonic anemometer has been explored.  
88 Known as *in situ* calibration, this approach has been tested by Singha and Sadr  
89 (2013) in measurements at the coastal region of Doha, Qatar, using a four-  
90 wire anemometer. In the proposed method, the calibration-data reduction is  
91 performed at once, and it uses the classical voltage-velocity relationship plus  
92 probe geometry information employed in the laboratory calibration in order  
93 to match the three sonic velocities with three hot-film voltages (the fourth val-  
94 idating wire was used in an error minimization function). Similarly, Frehlich  
95 et al. (2003) calibrated single hot-wire measurements using simultaneous data  
96 of the horizontal velocity from a Pitot tube vaned into the wind.

97 In a different approach, the calibration-data reduction developed by Kit  
98 et al. (2010) and Kit and Liberzon (2016) uses a shallow neural-network that  
99 is trained using the hot-film voltage and sonic velocity data measured simul-  
100 taneously, which is then used as a transfer function to convert the hot-film  
101 voltage into a high-frequency velocity time series. The combination of hot-  
102 film and sonic anemometer – known as a combo probe – has the additional  
103 advantage of automatically adjusting the sensors to the mean wind direc-  
104 tion, increasing its ability to provide continuous field measurements without  
105 human intervention. The neural-network calibration approach has been val-  
106 idated against traditional calibration using wind tunnel and field data (Kit  
107 et al. 2010; Kit and Liberzon 2016). When employed in the Mountain Terrain  
108 Atmospheric Modeling and Observations (MATERHORN) field experiment,  
109 Kit et al. (2017, 2021) used a combo probe calibrated with a neural network to  
110 investigate turbulent bursts and structure functions, respectively, within a 90-  
111 min period of stably stratified flow. Recent developments updated the combo  
112 probe calibration into a deep learning neural network approach (Goldshmid  
113 et al. 2022), eliminating the human-decision-based selection of data for the  
114 neural-network training, and improving its automatization.

115 In this study, we develop a new *in situ* calibration of a triple hot-film  
116 probe for the tower data of the CHATS experiment (Patton et al. 2011), with  
117 a focus on investigating the small-scale characteristics of the flow. In this par-  
118 ticular dataset, the sonic and hot-film sensors were positioned in proximity but  
119 pointing in different directions, and turbulence intensity is very often above  
120 the acceptable limit of the hot-film probe due to the measurement location's

close proximity to the CHATS canopy. We employ the traditional calibration method (voltage-velocity analytical equation plus geometric relationships), as this method allows explicit treatment of aforementioned misalignment of the probes and high turbulence intensity, and provides a direct result. The neural-network method, on the other hand, implicitly combines all features into a single numeric transfer function and may require rescaling of the hot-film velocity obtained. The calibration procedure performed here is similar to the one developed by Singha and Sadr (2013), except that the triple probe provides no additional information for error minimization and the classical voltage-velocity relationship has to be enforced exactly. We evaluate the ability of the triple hot-film in providing reliable information at the small scales by evaluating spectra and structure function ratios, which are very sensitive to measurement and calibration errors (as it will be discussed here) and have theoretical predictions for locally isotropic flows. Additionally, spectral densities and structure functions are also compared to the model spectra of Meyers and Meneveau (2008) and to the wind-tunnel data of Saddoughi and Veeravalli (1994), providing better insights on the quality of the hot-film data and on the characteristics of the small-scale atmospheric flow.

## 2 Methods

### 2.1 CHATS experiment

The Canopy Horizontal Array Turbulence Study (CHATS) is the third of the Horizontal Array Turbulence Study (HATS) experiments, which took place in the spring of 2007 in a deciduous walnut orchard near Dixon, California, USA, with the focus on investigating the main effects of plant canopies on atmospheric turbulence. In the experiment, crosswind arrays and a 30-m profile tower were instrumented with many turbulence, chemistry and meteorological sensors. Among those sensors, there were single hot-film anemometers mounted in the horizontal array and three triple hot-film anemometers mounted in the vertical array (at  $z/h = 0.6, 1$  and  $1.4$ , where  $h \approx 10$  m is the mean canopy height), all combined with Campbell Scientific CSAT3 sonic anemometers. In this study, we evaluate the data collected from the triple hot-film at  $z/h = 1.4$ , which is expected to have lower turbulence intensity (necessary for a better hot-film response) and to present atmospheric surface-layer characteristics with less impact of the canopy flow disturbances. The triple hot-film probe (quartz films covered with a thin nickel film by Dantec Dynamics, model 55R91) was mounted in the vertical support of the sonic arms at an approximately  $90^\circ$  angle relative to the main sonic streamwise direction (Fig. 1). The data set spans the period between May 13 and June 11 2007 (with-leaves period for the canopy).

Before proceeding with the data analysis, we note that within and above plant canopies, in the roughness sublayer, the flow is strongly impacted by the interaction between the turbulence and the canopy elements. Among other ef-

163 fects, the energy spectrum is altered by the production of eddies in the wake of  
 164 canopy elements, at the expense of the energy of larger eddies. This process has  
 165 been termed energy shortcut circuit (see Finnigan 2000) as some of the energy  
 166 of the large eddies bypass the energy cascade and gets transferred directly into  
 167 wake-scale eddies. This spectral-shortcut process causes distortions within the  
 168 inertial range, producing a faster decay at the larger scales and a bump at  
 169 around the wavenumber corresponding to the wake eddies (Finnigan 2000).  
 170 This feature is typically observed in one-dimensional spectra measured within  
 171 the canopy (e.g. Baldocchi and Meyers 1988; Amiro 1990; Cava and Katul  
 172 2008), whereas above the canopy one-dimensional spectra present a clear in-  
 173 ertial range with characteristics typical of the inertial layer (e.g. Shaw et al.  
 174 1974; Su et al. 2004; Mammarella et al. 2008). This inertial range behavior was  
 175 also observed at CHATS, as discussed by Dupont and Patton (2012, 2022). In  
 176 particular, the inertial range of the one-dimensional spectra showed very little  
 177 variation between  $z = 14$  m (height of the hot-film used here) and  $z = 29$  m  
 178 (a height which is outside of the roughness sublayer based on the results by  
 179 Pan and Chamecki, 2016, in particular for the shear-dominated atmospheric  
 180 stability condition considered here), thereby suggesting that canopy effects on  
 181 the small scales investigated here are limited to lower heights closer to canopy  
 182 top (located at  $z = 10$  m) and below. It is important to point out, however,  
 183 that 1D spectra can “smear” features otherwise present in two or three dimen-  
 184 sional spectra (Kelly and Wyngaard 2006), and the canopy has been shown  
 185 to impact 2D spectra in large-eddy simulation (LES) for  $z/h$  up to 2 (Patton  
 186 et al. 2016). Therefore, the potential impact of the canopy on the results dis-  
 187 cussed here cannot be ruled out. However, the objective of the present study  
 188 is to investigate the small-scale structures of the flow, which is reinforced by  
 189 the similarities with typical inertial-layer 1D spectra present in the literature.  
 190 Unfortunately, the quality of the hot-film data collected at  $z/h = 0.6$  and 1  
 191 does not allow for a similar investigation, including the canopy-induced spec-  
 192 tral features, due to the frequent violation of acceptable flow direction relative  
 193 to the fixed probe, and this analysis will be left for future studies.

## 194 2.2 Hot-film data processing

195 The geometry of the triple hot-film probe is such that each of the three films  
 196 is arranged as the edge of a cube, whose shared vertex points into the stream-  
 197 wise direction. The conversion from the measured voltages of each film ( $V_j$ ,  
 198 where  $j = 1, 2, 3$  identifies the films) to a velocity vector in the laboratory/field  
 199 cartesian coordinate system ( $u_{h,i}$ , where  $i = 1, 2, 3$  are the cartesian compo-  
 200 nents) starts with the use of a calibration curve in the form  $V_j^2 = a_j + b_j u_{p,j}^{0.45}$   
 201 known as King’s law, which provides the velocity vector in the films’ frame of  
 202 reference ( $u_{p,j}$ ). The second step is the conversion of the velocity vector to the  
 203 final frame of reference ( $i = 1, 2, 3$  for the streamwise, spanwise and vertical  
 204 directions), through the following matrix multiplications. First, the velocity  
 205 vector is corrected for yaw and pitch effects using



**Fig. 1** Left: picture of the sonic and hot-film sensors in the field (hot-film attached to the vertical support of the sonic arms in a 90° angle). Right: top view of the coordinate system of the sonic  $\langle u, v, w \rangle$  (pointing westward) and hot-film  $\langle X, Y, Z \rangle$  (pointing southward). We define the reference coordinate system as  $\langle u_1, u_3, u_2 \rangle$  and redefine the sonic and hot-film data accordingly.

$$\begin{pmatrix} u_{p,1}^{*2} \\ u_{p,2}^{*2} \\ u_{p,3}^{*2} \end{pmatrix} = \frac{1}{\alpha} \begin{pmatrix} k^4 - h_p^2 & h_p^4 - k^2 & 1 - h_p^2 k^2 \\ 1 - h_p^2 k^2 & k^4 - h_p^2 & h_p^4 - k^2 \\ h_p^4 - k^2 & 1 - h_p^2 k^2 & k^4 - h_p^2 \end{pmatrix} \begin{pmatrix} u_{p,1}^2 \\ u_{p,2}^2 \\ u_{p,3}^2 \end{pmatrix}, \quad (1)$$

206 in which  $\alpha = h_p^6 - 3h_p^2 k^2 + k^6 + 1$ ,  $k$  and  $h_p$  are the yaw and pitch coefficients,  
 207 respectively, and  $u_{p,j}^*$  is the corrected velocity vector in the films' frame of  
 208 reference. This relationship, which follows from the Jørgesen's directional re-  
 209 sponse equation, is general for any hot-film and provides the effective cooling  
 210 velocity as felt by each film when their yaw and pitch are taken into account  
 211 (Lekakis et al. 1989).

212 The second matrix multiplication, which provides the change in frame of  
 213 reference for the specific geometry of the sensor used here, can be written as

$$\begin{pmatrix} u_{h,1} \\ u_{h,3} \\ u_{h,2} \end{pmatrix} = \begin{pmatrix} 1/\sqrt{3} & 1/\sqrt{3} & 1/\sqrt{3} \\ -1/\sqrt{2} & 1/\sqrt{2} & 0 \\ 1/\sqrt{6} & 1/\sqrt{6} & -2/\sqrt{6} \end{pmatrix} \begin{pmatrix} u_{p,1}^* \\ u_{p,2}^* \\ u_{p,3}^* \end{pmatrix}. \quad (2)$$

214 Note that these relationships are presented as provided by the manufac-  
 215 turer (Jørgensen 2005), except for the redefinition of  $Y$  or 2 for spanwise and  $Z$   
 216 or 3 for vertical direction (in the original equations they are reversed). In addi-  
 217 tion to being different for each wire, these parameters may also be a function  
 218 of mean wind velocity (Lekakis et al. 1989). For better precision, the manufac-  
 219 turer recommends a calibration of these parameters in the lab, as they depend  
 220 mostly on the geometry of the probe, which may vary from probe to probe but  
 221 should not change during use (Jørgensen 2005). Since the manufacturer rec-  
 222 ommended calibration was not performed for this experiment and the probes  
 223 used were new, we use the manufacturer's values of  $k^2 = 0.04$  and  $h_p^2 = 1.2$ .

### 2.3 In-situ calibration from sonic anemometer data

In this study, sonic anemometer measurements are used to estimate the parameters for the King's law relationship between hot-film voltage and wind velocity for each 30-min period. For practical purposes we define the reference coordinate system as presented in Fig. 1. Note that the reference coordinate system follows the hot-film standard (to use the manufacturer's matrices) but reverses the name between the spanwise and vertical direction, to keep the nomenclature standard in the atmospheric community (i.e.,  $u_1, u_3, u_2$  corresponding to streamwise, vertical and spanwise directions). The measurement frequencies are 60 Hz and 2 kHz for sonic and hot-film, respectively. The first step for calibration is to obtain the effective cooling velocity of each film ( $u_{p,j}$ ) from the sonic raw data ( $u_{s,j}$ ). This is done by converting the sonic velocity to the films' frame of reference and accounting for the yaw and pitch effects, using the inverse matrices of the transformations (1) and (2), i.e.,

$$\begin{pmatrix} u_{p,1}^* \\ u_{p,2}^* \\ u_{p,3}^* \end{pmatrix} = \frac{1}{6} \begin{pmatrix} 2\sqrt{3} & -3\sqrt{2} & \sqrt{6} \\ 2\sqrt{3} & 3\sqrt{2} & \sqrt{6} \\ 2\sqrt{3} & 0 & -2/\sqrt{6} \end{pmatrix} \begin{pmatrix} u_{s,1} \\ u_{s,3} \\ u_{s,2} \end{pmatrix}, \quad (3)$$

and

$$\begin{pmatrix} u_{p,1}^2 \\ u_{p,2}^2 \\ u_{p,3}^2 \end{pmatrix} = \begin{pmatrix} k^2 & 1 & h_p^2 \\ h_p^2 & k^2 & 1 \\ 1 & h_p^2 & k^2 \end{pmatrix} \begin{pmatrix} u_{p,1}^{*2} \\ u_{p,2}^{*2} \\ u_{p,3}^{*2} \end{pmatrix}. \quad (4)$$

Now, the vector  $u_{p,j}$  comes from the sonic anemometer, and it can be compared to the voltage measured simultaneously by the hot-film. Note that due to the fact that the sensors are not collocated (Fig. 1), in addition to the path-averaging and other mechanical effects in the sonic anemometer, the higher frequencies of both signals can differ significantly. Therefore, in order to apply the King's law for each 30-min block, the two signals (sonic velocity and hot-film voltage) are low-pass filtered with a spectral cut-off filter at frequency of 0.05 Hz (a conservative choice). Based on the sonic's path-averaging alone, the cut-off frequency should be at most  $0.1\bar{u}_1/(2\pi p_l)$  (Horst and Oncley 2006), where  $p_l = 0.115$  m is the path length of the CSAT3. Therefore, the selected cut-off frequency will not violate the path-averaging requirement as long as  $\bar{u}_1 > 0.003$  m s<sup>-1</sup>. Note also that the velocity values available for calibration are dominated by the lower frequencies. After the obtention of the parameters  $a_j$  and  $b_j$ , the procedure described in Sec. 2.2 can be applied and hot-film velocity time series are obtained. Except for calibration, all other results presented here use the original data for both sensors (not low-pass filtered).

### 2.4 Initial data selection

In hot-film measurements, when the velocity vector falls outside the first octant of the  $u_{p,j}$  space (where all three velocity components are positive), a

problem known as rectification occurs, due to the inability of the hot-film to distinguish the direction of the velocity vector (Maciejewski and Moffat 1994). Furthermore, in Eq. (1), the square of the corrected velocity  $u_{p,j}^*$  is related to the square of the effective cooling velocity  $u_{p,j}$ , disregarding directional information. In this relationship, a square-root of a negative term can occur when one of the three velocity components of  $u_{p,j}$  is sufficiently different from the other two. If the three films always point into the streamwise direction, the three velocity components  $u_{p,j}$  should be of similar magnitude. However, due to fluctuations in wind direction and intensity, it is very common to have a square root of a negative number, creating gaps in the time series. Therefore, by using this calibration approach, the presence of gaps guarantee that no data contamination caused by the incorrect wind direction is present in the final dataset.

Fortunately, this is not an issue in the calibration step, since in the conversion of sonic data into the films' frame of reference there is no mechanism to produce a negative radicand (Eq. (4)). Furthermore, the low-pass filtering of the calibration step significantly reduces these fluctuations. For that reason, the calibration step is performed for each 30-min block. However, the final hot-film time series is generated as smaller subblocks of data between the gaps (see Fig. 12 in the Appendix). Note that we cannot perform calibration for small subblocks of data (potentially excluding the gaps) because the calibration step relies on the low-frequency similarity between the two sensors. The final subblocks of data also do not present rectification issues, as observed *a posteriori*.

Because the hot-film probe needs to be pointed into the streamwise wind direction, we started by selecting 30-min blocks of data whose mean wind direction is within a  $10^\circ$  cone from the hot-film streamwise direction. By setting the minimum size of the subblock to 30-seconds, we further select blocks that have a minimum of 25 subblocks, in order to obtain turbulence statistics with reduced scatter from the average across subblocks (see illustration in the Appendix).

Finally, we note that, by using this calibration approach, we were able to observe that the calibration is very sensitive to errors in the alignment between the hot-film probe and the sonic anemometer. From the experimental setup, we noticed that there is a  $180^\circ$  rotation about the hot-film  $X$ -axis (i.e., the probe was mounted "upside-down"), which is taken into account when processing the raw data by multiplying the vector by a rotation matrix. We do not expect any rotation about the spanwise axis of the hot-film due to the type of mounting support used (see Fig. 1), but a small rotation about the vertical axis is possible. During the experiment, the hot-film and sonic anemometers were deployed with an estimated  $90^\circ$  rotation about the vertical axis between them (measured by hand with a magnetic compass). Assuming that this  $90^\circ$  rotation about the vertical axis is accurate, we observe that velocity derivative variances from the blocks selected using the criteria defined above all exhibit a bias from the expected behavior for isotropic flows ( $\overline{(\partial u_i / \partial x_1)^2} / \overline{(\partial u_1 / \partial x_1)^2} = 2, i = 2, 3$ , estimated using Taylor's frozen tur-

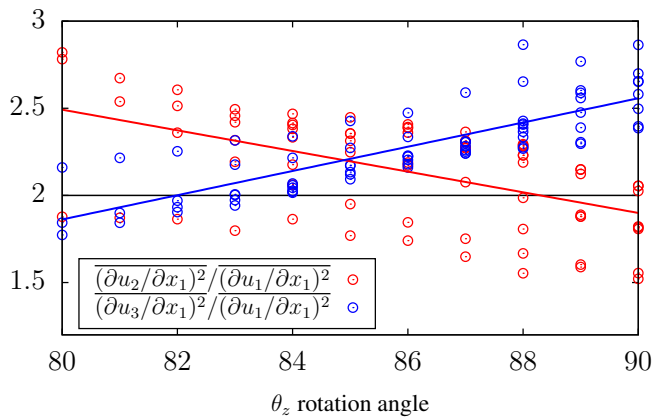


**Fig. 2** Ratios of the velocity derivative variances ( $\frac{(\partial u_2 / \partial x_1)^2}{(\partial u_1 / \partial x_1)^2}$  in red,  $\frac{(\partial u_3 / \partial x_1)^2}{(\partial u_1 / \partial x_1)^2}$  in blue) as a function of the rotation angle about the hot-film vertical axis ( $\theta_z$ ). Horizontal black line corresponds to the theoretical value of 2, and red and blue lines correspond to the linear fit of each ratio as a function of  $\theta_z$ . Each pair of circles correspond to the result for a different 30-min block that passed the selection criteria.

304 bulence hypothesis after subtraction of the mean velocity). As mentioned by  
 305 Gulitski et al. (2007), large deviations from local isotropy in the context of  
 306 hot-film measurements in the atmospheric boundary layer are likely an indica-  
 307 tion of calibration error rather than a real physical phenomenon. For this  
 308 reason, we tested the impact of taking into account a small rotation error  
 309 about the vertical axis of the hot-film ( $\theta_z$  in Fig. 1), and the result showed  
 310 a clear trend of the ratios as a function of  $\theta_z$  (Fig. 2). This is in accordance  
 311 with the assumption of cross-contamination between the velocity components  
 312 due to misalignment between sensors. The trend indicates that the most likely  
 313 correct position corresponds to  $\theta_z = 85^\circ$ , when the isotropy ratios are similar  
 314 to each other (although biased toward  $\sim 2.2$ , possibly due to the anisotropy  
 315 in the spectral bump, see discussion in Sec. 4.1). We adopt this angle (instead  
 316 of the originally reported  $90^\circ$  angle) during hot-film calibration also using a  
 317 rotation matrix. This is an example of how sensitive the results can be to small  
 318 experimental errors.

## 319 2.5 Final data selection

320 Very few 30 min blocks of data satisfied the stringent wind angle require-  
 321 ments for the hot-film probe calibration to be reliable during most of the  
 322 block (i.e. within  $\pm 10^\circ$  of  $\theta_z$ ). For that reason, no additional quality-control  
 323 test needed to be performed in the data. Most blocks satisfying the criteria oc-  
 324 curred in the early hours of June 10, spanning a continuous period of 3 hours.  
 325 Due to their similar flow conditions (see Appendix), and in order to increase  
 326 the subblock size and reduce data scatter, we combined them into a single 3-

hour block from 03:30h to 06:30h local time. Table 1 provides the flow statistics for this block, which has a mean wind of  $2.21 \text{ m s}^{-1}$  in a  $5.94^\circ$  angle, and corresponds to weakly stable condition (stability parameter  $(z - d_o)/L_o = 0.29$ , where  $d_o$  is the canopy displacement height and  $L_o$  is the Obukhov length, see Tab. 1 for details). The turbulence intensity, defined as  $k^{1/2}/\bar{u}_1$ , is equal to 0.22, which is above the 0.15 limit of the probe (Jørgensen 2005) and explains the large number of error gaps. A single calibration is performed for the entire 3 hour period (see Fig. 3). Notice the agreement in the low-frequencies between the compensated hot-film voltage and sonic velocity spectra rotated into the films' frame of reference. The deviations in the high-frequency range result from limitations of the sonic anemometer in this frequency range (path-averaging and aliasing, for example), and start around 0.3 Hz, as expected for the path-averaging attenuation ( $0.1\bar{u}_1/(2\pi p_l) = 0.31 \text{ Hz}$ , Horst and Oncley (2006)). We note that reproducing all statistics presented here using a cut-off frequency of 0.3 Hz generates no relevant differences in our results or conclusions (not shown). As these spectra are in the hot-films's frame of reference, they are dominated by the streamwise velocity component. The presence of an inertial range is already clear in the hot-film data, and the limitation of the corresponding sonic data is also already visible. In interpreting sonic data presented here, it is important to bear in mind that the  $85^\circ$  arrangement is likely impacting the quality of the sonic result, as it will be discussed in the next section. Furthermore, we have decided not to use the transducer shadowing correction proposed by Horst et al. (2015), because the attenuation for the variances is small and very similar for all three components for a wind direction close to  $90$  degrees. In addition, the effect of the correction on the CSAT3 sonic anemometer spectra has been shown to generate only a small improvement on the inertial range isotropy ratios, even for small wind directions (Peña et al. 2019).

From this calibration, 33 subblocks of 2-min data were obtained, which were averaged to provide the results presented next. Because a 2-min sample size can be small compared to the integral time scale, tapering the time series is recommended to compensate for the sample size effect on the spectra (Kaimal and Finnigan 1994). However, when comparing the 2-min sonic spectra to the original 3-hour spectra, the spectral loss was negligible for the analyses performed here, and tapering the time-series using a Hamming window (as suggested by Kaimal and Finnigan (1994)) had virtually no effect (not shown). Therefore, tapering was also not included in the final analyses.

A sample of the final velocity time series from the hot-film and sonic data is presented in Fig. 4. Although some discrepancies can be observed in certain data intervals, the large-scale fluctuations are very similar between the two sensors. As expected, clear differences in the small scales are easily identified when the time series are displayed in details (inset of Fig. 4). A comparison of the two filtered time series is provided in the Appendix.

Table 1 also provides some statistics from the average of the 33 2-min subblocks, including the flow variances and Kolmogorov and Taylor length scales. The selected data correspond to a Taylor Reynolds number  $Re_\lambda =$

**Table 1** Flow parameters for the selected block (06/10/2007 03:30h–06:30h):  $(z - d_o)/L_o$  is the Obukhov stability parameter, in which  $z = 14$  m is the measurement height,  $d_o \approx 0.75h = 7.5$  m is the canopy displacement height (estimated for this canopy under near-neutral conditions by Shapkalijevski et al. (2016)),  $h \approx 10$  m is the canopy height and  $L_o = 22.7$  m is the Obukhov length. The mean wind velocity  $\bar{u}_1$ , friction velocity  $u_*$ , turbulent kinetic energy  $k$ , turbulence intensity  $TI = k^{1/2}/\bar{u}_1$ , velocity standard deviation  $\sigma_i$  and heat flux  $w'\theta'$  were measured at 1.4h. Primes indicate fluctuations from the block average (overbar). The mean wind direction is relative to the reference  $u_1$  direction (hot-film axis).  $a_j, b_j$  are the King’s law parameters for film  $j$ .  $\varepsilon$  from the integral of the dissipation spectrum (average of the three components, Eq. (5)),  $\nu = 15.16 \times 10^{-6} \text{ m}^2 \text{ s}^{-1}$ ,  $\eta = (\nu^3/\varepsilon)^{1/4}$ ,  $\lambda = u'(15\nu/\varepsilon)^{1/2}$ ,  $Re_L = k^2/(\varepsilon\nu)$ ,  $Re_\lambda = u'\lambda/\nu = (20Re_L/3)^{1/2}$ , where  $k = (\overline{u_1'^2} + \overline{u_2'^2} + \overline{u_3'^2})/2$  is the turbulent kinetic energy and  $u' = (2k/3)^{1/2}$  is the Taylor velocity scale (Pope 2000).

Statistics of the entire 3h-block	
$z/h$	1.4
$\bar{u}_1$ (m s <sup>-1</sup> )	2.21
mean wind direction (°)	5.94
$u_*$ (m s <sup>-1</sup> )	0.21
$k$ (m <sup>2</sup> s <sup>-2</sup> )	0.23
$TI$	0.22
$w'\theta'$ (K m s <sup>-1</sup> )	-0.03
$(z - d_o)/L_o$	0.29
Calibration	
$a_1, b_1$	1.35, 2.23
$a_2, b_2$	1.24, 2.24
$a_3, b_3$	1.35, 2.25
Statistics of the average of the 33 2-min subblock	
$\sigma_1, \sigma_2, \sigma_3$ (m s <sup>-1</sup> )	0.37, 0.34, 0.28
$\varepsilon$ (m <sup>2</sup> s <sup>-3</sup> )	$4.88 \times 10^{-3}$
$\eta$ (mm)	0.919
$\lambda$ (cm)	7.12
$Re_\lambda$	1550
$Re_L$	$3.6 \times 10^5$

1550. The mean dissipation rate was estimated from the average of the values  
 374 obtained from the numerical integral of each dissipation spectrum, i.e.,

$$\varepsilon = \frac{1}{3} \left\{ 15\nu \int_{k_{1,0}}^{k_{1,\infty}} k_1^2 E_{11}(k_1) dk_1 + \frac{15}{2} \nu \int_{k_{1,0}}^{k_{1,\infty}} k_1^2 E_{22}(k_1) dk_1 + \frac{15}{2} \nu \int_{k_{1,0}}^{k_{1,\infty}} k_1^2 E_{33}(k_1) dk_1 \right\}, \quad (5)$$

375 in which  $[k_{1,0}, k_{1,\infty}]$  is the streamwise wavenumber interval with available  
 376 data. Taylor’s frozen turbulence hypothesis was used to convert frequency  
 377 into wavenumber.

378 Regarding the use of the Taylor’s frozen turbulence hypothesis in high-  
 379 frequency turbulence measurements, it is important to take into account the  
 380 possible errors caused by the fluctuating advection velocity, as evaluated for  
 381 example by Wyngaard and Clifford (1977). The corrections proposed by Wyn-  
 382 gaard and Clifford (1977) correspond to constant factors applied to the veloc-  
 383 ity derivative variances and spectra, which are a function of the turbulence

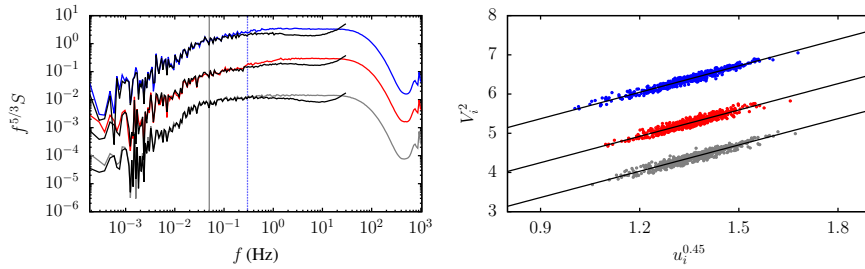


**Fig. 3** (a) Hot-film voltage (color lines) and sonic velocity (black lines) compensated spectra in the hot-film frame of reference (all three components in  $\approx 35^\circ$  angle with the streamwise direction); (b) King's law calibration curve (dots are data, line is the best linear fit), for each film (1-grey, 2-red, 3-blue, 2 and 3 are vertically shifted). Spectra were smoothed using bin averages in log scale. The match between voltage and velocity spectra is obtained by vertically shifting the voltage spectra manually, in order to show that they behave similarly (absolute values are not relevant). Vertical lines corresponds to the low-pass filter cut-off frequency used to select the calibration curve data (0.05 Hz, solid black line) and the cut-off frequency limitation from the sonic path-averaging (0.3 Hz, dashed blue line).

384 intensity and were estimated assuming Kolmogorov's inertial range model for  
 385 the spectrum. The respective correction factors for  $(\partial u_i / \partial x_1)^2$  estimated for  
 386 this dataset are 0.911, 0.952, 0.948 for  $i = 1, 2, 3$ , respectively. These correc-  
 387 tions would reduce the value of  $\varepsilon$  by 7%. The correction factors for  $E_{\alpha\alpha}$  are  
 388 0.979, 0.996, 0.994 for  $\alpha = 1, 2, 3$  respectively, which has a negligible effect on  
 389 isotropy ratios. Because these corrections are within the variability of the 33  
 390 subblocks and they do not impact any analysis or conclusion of this study,  
 391 we chose to not include the corrections. Finally, we note that the sensor's  
 392 length of  $l_h = 1.25 \text{ mm} = 1.36\eta$  is not expected to introduce attenuation at  
 393 the dissipation scales for these data.

### 394 3 Reference data

#### 395 3.1 Saddoughi and Veeravalli (1994)

396 Turbulence measurements from a wind-tunnel experiment with  $Re_\lambda$  up to  
 397 1500 were obtained in the Full-Scale Aerodynamics Facility at NASA Ames  
 398 Research Center, in which a boundary layer developed over a rough surface.  
 399 The dataset resulting from this experiment has been a reference for boundary-  
 400 layer flows since its publication (Pope 2000), as it provided at the time the  
 401 highest Reynolds number ever attained in a wind-tunnel. These results com-  
 402 prised spectra and second- and third-order structure functions, including their  
 403 ratios, providing evidence of a locally isotropic flow, with exponential decay  
 404 at the dissipation range and the presence of spectral bumps at the transition  
 405 between the inertial and dissipation scales.

406 In this study we selected the  $Re_\lambda = 1450$  data as a reference, due to the  
 407 similar  $Re_\lambda$  value compared to the CHATS data. The selected data set cor-

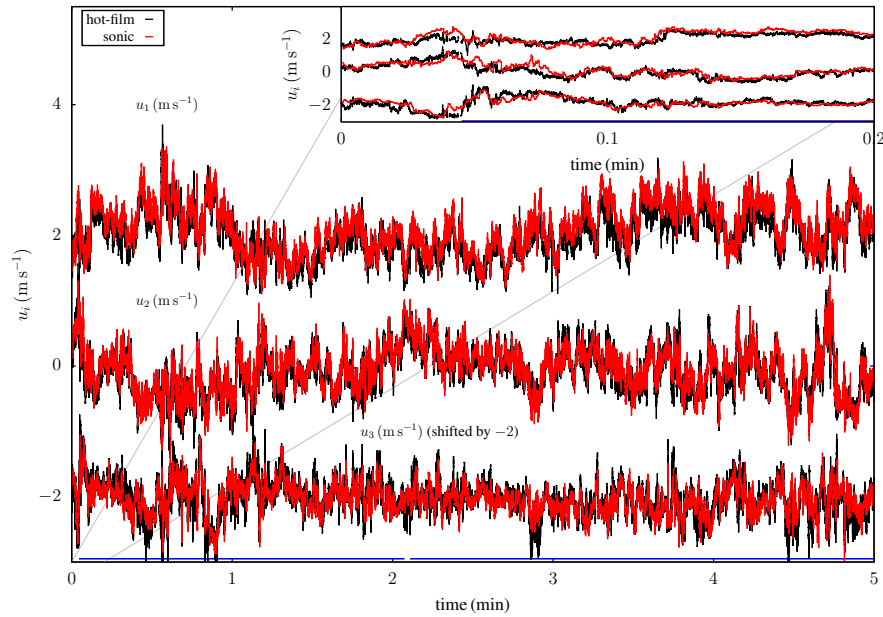


**Fig. 4** Sample of velocity time series from sonic (red) and hot-film (black) anemometers, starting at June 10 03:30h local time. Inset is a closer look into the first 12 seconds. Blue lines at the bottom indicate the 2-min subblocks without data gaps for this sample.

408 responds to their mid-layer high-speed case (the distance from the ground is  
 409 400 mm, note that Saddoughi and Veeravalli (1994) use  $y$  to represent vertical  
 410 distance). The value of  $\varepsilon = 49 \pm 10\% \text{ m}^2\text{s}^{-3}$  was estimated using the Kol-  
 411 mogorov's law for the inertial range with  $C_k = 1.5$ , as a direct estimate was  
 412 not possible for that specific case. The value of  $C_k = 1.5$  was derived based  
 413 on the compensated spectra of the mid-layer low-speed case ( $Re_\lambda \approx 600$ ),  
 414 which had  $\varepsilon = 0.33 \pm 10\% \text{ m}^2\text{s}^{-3}$  estimated from the integral of the dissipa-  
 415 tion spectra. These values were used to nondimensionalize their compensated  
 416 spectra. Using their third-order structure functions, the values of  $\varepsilon$  were esti-  
 417 mated as about 20% lower for both low and high-speed cases ( $\varepsilon = 0.26$  and  
 418  $40 \text{ m}^2\text{s}^{-3}$ , corresponding to  $Re_\lambda = 670$  and 1500, respectively), which they  
 419 used to nondimensionalize their second and third-order structure functions. In  
 420 here, we used this estimate from the third-order structure function to plot all  
 421 their results, i.e., we re-nondimensionalized their spectra results in order to  
 422 maintain consistency between spectra and structure function (we chose this  
 423 estimate as it does not rely on the  $C_k$  value, which can be contaminated by  
 424 the low Reynolds number of the  $Re_\lambda \approx 600$  case, see discussion in Sec. 4.3).

### 3.2 Meyers and Meneveau (2008)

To help with data interpretation, we use the model three-dimensional spectrum proposed by Meyers and Meneveau (2008). The model updates previous theoretical models based on the inertial and dissipation decay rates by incorporating the bottleneck and intermittency effects as observed in DNS, laboratory and atmospheric data. The three dimensional spectrum  $E(\kappa)$  is defined as the contribution to the turbulent kinetic energy from all wavenumbers with absolute value  $\kappa$ , and the proposed model corresponds to

$$E(\kappa) = C_k \varepsilon^{2/3} \kappa^{-5/3} (\kappa L)^{-\beta} f_L(\kappa L) f_\eta(\kappa \eta), \quad (6)$$

$$f_L(\kappa L) = \left\{ \frac{\kappa L}{[(\kappa L)^p + \alpha_5]^{1/p}} \right\}^{5/3+\beta+2}, \quad (7)$$

$$f_\eta(\kappa \eta) = \exp(-\alpha_1 \kappa \eta) \left[ 1 + \frac{\alpha_2 (\kappa \eta / \alpha_4)^{\alpha_3}}{1 + (\kappa \eta / \alpha_4)^{\alpha_3}} \right], \quad (8)$$

in which  $C_k$  is the Kolmogorov constant,  $\varepsilon$  is the turbulence kinetic energy dissipation rate,  $L$  is the integral length scale,  $\beta$  is the intermittency correction for the inertial-range slope,  $\eta = (\nu^3/\varepsilon)^{1/4}$  is the Kolmogorov (dissipation) length scale, in which  $\nu$  is the kinematic viscosity, and  $f_L$  and  $f_\eta$  are non-dimensional functions representing the integral and dissipation scales, respectively. The main contributions from this approach compared to other spectrum models (such as Pope (2000)'s) are the parameterization of the intermittency and bottleneck effects, the later being the spectral bump at the transition between the inertial and dissipation scales (modeled by the term multiplying the exponential function in Eq. (8)).

In addition to the flow scales and parameters, the values of  $\alpha_1$ – $\alpha_5$  need to be determined in order to close the model. For a given Reynolds number, five flow constraints are used to obtain these constants, namely the total energy, enstrophy and palinstropy from their corresponding integrals of the energy spectrum ( $E(\kappa)$ ,  $\kappa^2 E(\kappa)$  and  $\kappa^4 E(\kappa)$ , respectively), combined with the constraint for the magnitude and location of the intermittency corrected dissipation peak (equations 6-8 and 11 of the original study). From the field data we extract the Reynolds number, dissipation rate, and the derivative skewness  $S_3$  (needed for the palinstropy constraint, see Meyers and Meneveau (2008) for details). The values of  $p = 1.5$ ,  $\beta = \mu/9$  ( $\mu = 0.25$  is the standard empirical value of intermittency exponent) were selected as in Meyers and Meneveau (2008). The value of the Kolmogorov constant  $C_k = 2.3$  was used as in the modeling of atmospheric data from Tsuji (2004) by Meyers and Meneveau (2008). Table 2 provides the model parameters for the present data in addition to the results of the field data provided by Tsuji (2004) (discussed in Sec. 4.3), obtained using the GNU Octave software (Eaton et al. 2020).

Note that from this model, the behavior in the inertial range deviates from Kolmogorov's law, especially if the Reynolds number is very large (so that  $\kappa L$  is large in the inertial range). However, if the spectrum is normalized according to Kolmogorov's law, it will require a different constant, i.e.,  $E(\kappa) = C'_k \varepsilon^{2/3} \kappa^{-5/3}$ .

Here,  $C'_k = C_k(\kappa_{\text{IR}}L)^{-\beta}f_\eta(\kappa_{\text{IR}}\eta)$  and  $\kappa_{\text{IR}}$  is a wavenumber representative of the inertial range (Meyers and Meneveau 2008). Therefore, the value of  $C_k = 2.3$  should not be used directly in Kolmogorov's law.

From Meyers and Meneveau (2008)'s model, the following relations are used to obtain the one-dimensional energy spectra (the contribution of the streamwise wavenumber  $k_1$  to each corresponding variance) and second- and third-order structure functions for each velocity component (Pope 2000):

$$E_{11}(k_1) = \int_{k_1}^{\infty} \frac{E(\kappa)}{\kappa} \left(1 - \frac{k_1^2}{\kappa^2}\right) d\kappa, \quad (9)$$

$$E_{22}(k_1) = E_{33}(k_1) = \frac{1}{2} \left( E_{11}(k_1) - k_1 \frac{dE_{11}(k_1)}{dk_1} \right), \quad (10)$$

$$D_{\gamma\gamma}(r_1) = 2 \int_0^{\infty} E_{\gamma\gamma}(k_1) [1 - \cos(k_1 r_1)] dk_1, \quad \gamma = 1, 2 \text{ or } 3, \quad (11)$$

$$D_{111}(r_1) = -\frac{4}{5}\varepsilon r_1 + 6\nu \frac{dD_{11}(r_1)}{dr_1}, \quad (12)$$

$$D_{122}(r_1) = D_{133}(r_1) = \frac{1}{6} \left( r_1 \frac{dD_{111}(r_1)}{dr_1} + D_{111}(r_1) \right), \quad (13)$$

in which  $r_1$  is the separation distance in the longitudinal direction. The structure functions are defined as

$$D_{\gamma\gamma} = \overline{[u_\gamma(x_1 + r_1) - u_\gamma(x_1)]^2} \quad (14)$$

$$D_{\gamma\omega\omega} = \overline{[u_\gamma(x_1 + r_1) - u_\gamma(x_1)][u_\omega(x_1 + r_1) - u_\omega(x_1)]^2}. \quad (15)$$

Note that Eqs. (9), (10) and (13) are only valid for locally homogeneous and isotropic flows, whereas Eq. (12), from the Kármán-Howarth equation, requires the additional constraint of stationarity (Hill 1997). Therefore the model predictions presented here are only meaningful within the scales for which local isotropy is a reasonable assumption. All hot-film results presented next are accompanied by model predictions to facilitate the discussion.

## 4 Results

The one-dimensional spectra in the streamwise direction for each velocity component are presented in Fig. 5. As done in previous *in situ* calibration studies (Kit et al. 2010; Singha and Sadr 2013), visual inspection of the spectra combined with the time series of Fig. 4 indicates a successful calibration. A quantitative error estimation is provided in the Appendix, showing that, although the sonic data is not an ideal "ground truth" velocity in this case due to the sensors' misalignment, the errors are in the range of previous *in situ* calibration studies. Here, a more detailed comparison of the small scales is provided, including compensated spectra and structure functions and isotropy ratios, presented in log-linear graphics (as opposed to log-log graphics typically used in the literature) in order to emphasize similarities and discrepancies. Note that

**Table 2** Parameters of the Meyers and Meneveau (2008)'s model estimated for the present data and for the data from Tsuji (2004). As in Meyers and Meneveau (2008), the values of  $C_k = 2.3$ ,  $p = 1.5$ ,  $\beta = \mu/9$  and  $\mu = 0.25$  were used, in addition to the measured value of  $S_3$  for the present data (italic), and calculated from  $S_3 = C_3 Re_\lambda^{9\mu/16}$  for  $C_3 = -0.146$  (upper bound, corresponding to the  $S_3$  measured in this study) and  $-0.218$  (lower bound, corresponding to the value used by Meyers and Meneveau (2008) for Tsuji (2004)'s data). Mean velocity  $\bar{u}_1$  in  $[\text{m s}^{-1}]$  and mean dissipation rate  $\varepsilon$  in  $[\text{m}^2 \text{s}^{-3}]$ .

	present	Tsuji (2004)			
$\bar{u}_1$	2.21	2.82	5.16	5.67	7.66
$\varepsilon$	0.00488	0.0106	0.0840	0.0598	0.0760
$Re_\lambda$	1550	5940	12240	15630	21180
Upper bound					
$S_3$	<i>-0.41</i>	-0.50	-0.55	-0.57	-0.59
$\alpha_1$	6.64352	5.42477	4.96725	4.83118	4.67283
$\alpha_2$	9.57462	4.14483	3.11842	2.87126	2.61096
$\alpha_3$	1.53194	1.73657	1.89901	1.96447	2.05451
$\alpha_4$	0.31066	0.17458	0.14447	0.13712	0.12945
$\alpha_5$	5.73480	5.80286	5.82066	5.82470	5.82867
Lower bound					
$S_3$	-0.61	-0.74	-0.82	-0.85	-0.88
$\alpha_1$	4.46575	4.00902	3.79519	3.72710	3.64518
$\alpha_2$	1.74661	1.44918	1.32980	1.29424	1.25301
$\alpha_3$	6.43234	10.55001	15.49512	18.24595	23.17269
$\alpha_4$	0.12115	0.12863	0.13551	0.13835	0.14227
$\alpha_5$	5.57008	5.76794	5.80600	5.81379	5.82113

490 the range of the spectra used for calibration of the hot-film data ( $f \leq 0.05$  Hz)  
491 is barely included in the data analysis presented hereafter (see Fig. 5), because  
492 the size of the subblocks (2 min) limits estimates of such low frequencies (see  
493 Appendix for further discussion).

#### 494 4.1 Spectra

495 Figure 6 compares dissipation spectra between hot-film and Meyers and Meneveau  
496 (2008)'s model for each velocity component. Since they were independently derived,  
497 the similar behavior between model and observations serve as another indication of  
498 the successful data calibration. It also shows that the model captures fairly well the  
499 position and shape of the peaks in dissipation, which are associated with the spectral  
500 bump at  $k_1 \eta \approx 0.1$ . By construction, the model and data should have the same total  
501 rate of dissipation (as this is one of the input parameters used in the model). Because  
502 the model assumes isotropy, the overprediction in the streamwise component (mostly  
503 compensated by under prediction in the spanwise component, Fig. 6(a,b)) signals  
504 deviations from isotropy at the dissipation scales in the hot-film data. This is  
505 in part associated with properties of the spectral bump as discussed further  
506 below.

508 When the energy spectra are compensated using Kolmogorov's scaling (i.e.,  
509 premultiplied by  $k_1^{5/3}$ ), we can identify roughly one decade of inertial range

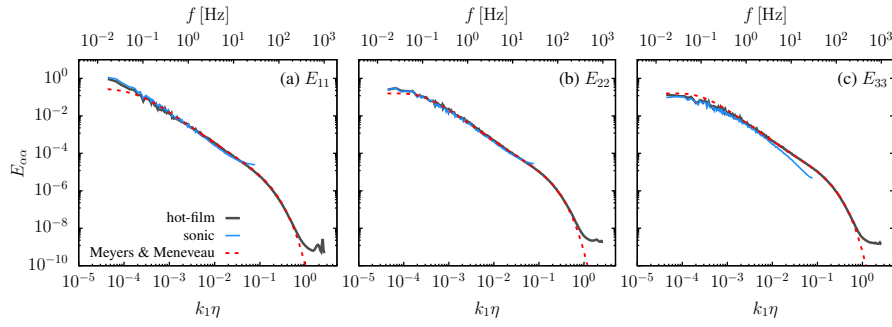


**Fig. 5** One-dimensional spectra for the (a) streamwise, (b) spanwise and (c) vertical velocities as a function of the streamwise nondimensional wavenumber and frequency. Spectra were smoothed using bin averages in log scale, and Taylor’s frozen turbulence hypothesis was used. Hot-film (grey) and sonic (blue) anemometers data, in addition to Meyers and Meneveau (2008)’s model (dashed red lines).

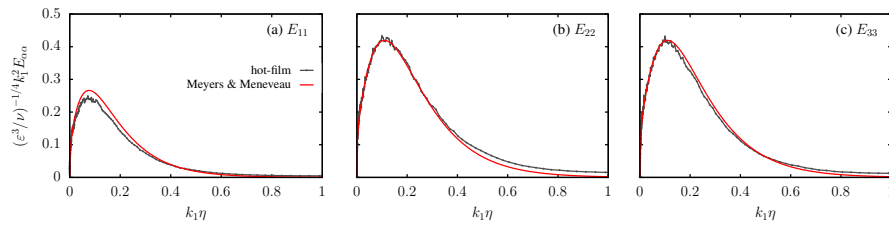


**Fig. 6** Dissipation spectra for the (a) streamwise, (b) spanwise and (c) vertical velocities as a function of the nondimensional wavenumber. Hot-film data in grey and Meyers and Meneveau (2008)’s model in red. The mean dissipation rate was estimated as the average of the integrals of these three data curves (Eq. (5)).

510 behavior in the streamwise component (Fig. 7(a)), which does not seem to display a spectral bump. In the other two components (Fig. 7(b-c)), the presence  
 511 of spectral bumps prevent the formation of a clear inertial range at this fairly  
 512 low Reynolds number. When comparing spectra from the sonic with those from  
 513 hot-film, the sonic path-averaging and aliasing effects become quite clear, the  
 514 former being most significant in the vertical component (which has the larger  
 515 path length). It is important to emphasize that the errors associated with sonic  
 516 anemometer, including path averaging (Horst and Oncley 2006) and flow distortion  
 517 by transducer shadowing (Horst et al. 2015), are influenced by the  
 518 incident wind angle, and the  $\sim 90^\circ$  angle used in this study enhances the  
 519 degradation of the sonic data (these errors tend to be substantially smaller  
 520 for angles within  $\pm 45^\circ$ ). For that reason, we avoid placing too much emphasis  
 521 on the limitations of the sonic anemometer as a more meaningful comparison  
 522 would require both sensors to be pointing in the same direction (so that the  
 523 incidence angle is the same).  
 524

525 The best comparison between data and model is also given by the compensated  
 526 spectra (premultiplied  $\kappa_1^{5/3+\beta}$  in Fig. 7(d-f)). Note that here we use the  
 527 intermittency correction in the compensated spectra to properly identify the

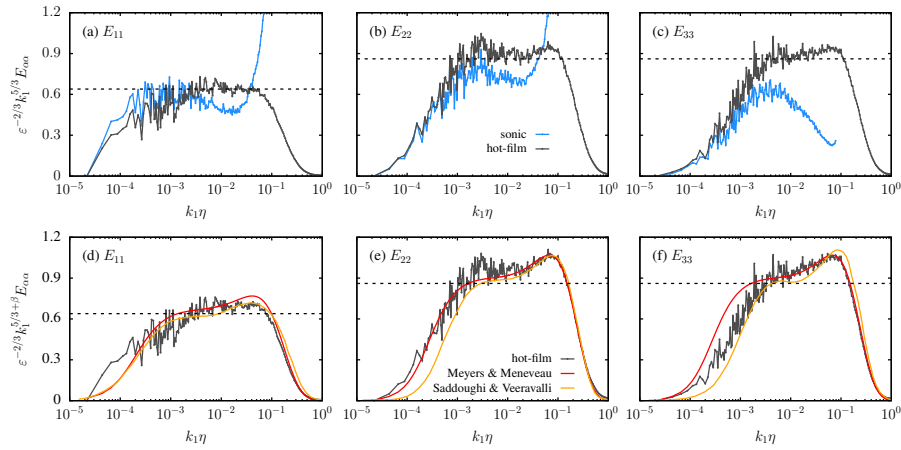


**Fig. 7** Compensated one-dimensional spectra of (a,d) streamwise, (b,e) spanwise, (c,f) vertical velocities as a function of the nondimensional wavenumber. Hot-film/sonic data in grey/blue lines, Meyers and Meneveau (2008)’s model and Saddoughi and Veeravalli (1994)’s data in red/yellow lines. The dashed black horizontal lines correspond to the theoretically predicted values for the inertial range.

528 existence of the inertial range in the model. While the model predicts a bump  
 529 in all three velocity components (less pronounced in  $E_{11}$ ), the data follows  
 530 the model closely in the large wavenumbers only in the spanwise and vertical  
 531 directions, for which a clear spectral bump is present. The lack of a bump  
 532 in  $E_{11}$  obtained from the hot-film, whose cause cannot be inferred from this  
 533 data set, is likely influencing the observed dissipation spectra anisotropy and  
 534 the 2.2 value obtained for the isotropy ratios of the velocity derivative variance  
 535 (Fig. 2), since the peak in the dissipation spectra approximately coincides  
 536 with the end of the peak in the bump. Except for the lack of a spectral bump  
 537 in  $E_{11}$ , the only other clear difference between the data and the model is in  
 538 the energy-containing range ( $k_1\eta \lesssim 10^{-3}$ ) for  $E_{33}$ , where the hot-film closely  
 539 follows the sonic. This reduction in the energy-containing scales of  $E_{33}$  is ex-  
 540 pected as the vertical velocity is significantly impacted by the blocking of the  
 541 flow by the ground, making the integral scales quite anisotropic and violating  
 542 the model assumptions in this range of scales. Figure 7 also includes an empiri-  
 543 cal fit to the wind-tunnel data (ninth-order, least-square, log-log polynomial  
 544 fits) as presented by Saddoughi and Veeravalli (1994). Compared to the atmo-  
 545 spheric data with similar  $Re_\lambda$  evaluated here, the Saddoughi and Veeravalli  
 546 (1994) data presents a more pronounced bump in both streamwise and verti-  
 547 cal components and some differences in the production range, but the overall  
 548 agreement with the model is quite good.

549 The ratios between components of the one-dimensional spectra are usu-  
 550 ally employed to assess the validity of local isotropy and are presented in  
 551 Fig. 8, which further characterizes the inertial range behavior and the simi-  
 552 larity between hot-film data and Meyers and Meneveau (2008)’s model. The

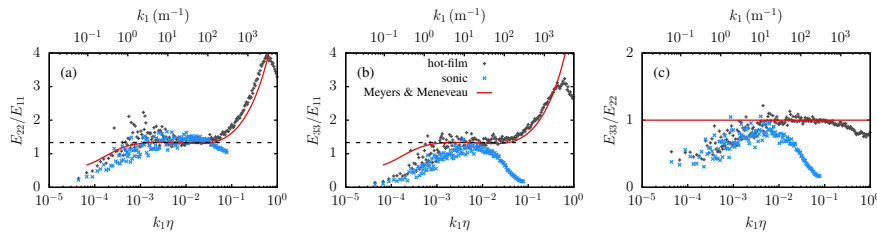


**Fig. 8** Ratios of the one-dimensional spectra. Hot-film/sonic anemometers data in grey/blue crosses, in addition to Meyers and Meneveau (2008)’s model (red lines). The dashed black horizontal lines correspond to the theoretically predicted  $4/3$  value for the inertial range.

553 local isotropy predictions for the inertial range ( $E_{22}/E_{11} = E_{33}/E_{11} = 4/3$   
 554 and  $E_{33}/E_{22} = 1$ ) are also indicated. Note that the isotropic model predicts  
 555 the ratios between transverse components to the streamwise component to be  
 556 larger than  $4/3$  in the dissipation range. In general, the agreement between  
 557 data and model in the inertial range and in the dissipation range confirm that  
 558 the local isotropy assumption is reasonably justified. The sonic anemome-  
 559 ter seems to have limitations that prevent an adequate assessment of local  
 560 isotropy, especially when the vertical component is included. This conclusion  
 561 was also obtained by Peña et al. (2019), in particular for the Campbell CSAT3  
 562 anemometer, whose ratio  $E_{33}/E_{11}$  was at most 1.2 even after accounting for  
 563 flow-distortion effects. Therefore, if this type of behavior for sonic data is  
 564 confirmed at larger Reynolds numbers and different angles of incidence, then  
 565 caution should be taken when using CSAT3 in the assessment of local isotropy  
 566 in the inertial range.

#### 567 4.2 Structure functions

568 Evaluation of the second-order structure function is more sensitive to small  
 569 differences between sonic, hot-film, and model results, given that it corresponds  
 570 to an integral of the spectrum (Eq. (11)). Figure 9 (upper panels) reinforces  
 571 the similarity between hot-film, model and wind-tunnel data in the dissipation  
 572 range, in addition to the similarity between hot-film and model across all scales  
 573 in the spanwise component  $D_{22}$ . The discrepancies discussed in the context  
 574 of the spectra are amplified here. The absence of a spectral bump in  $E_{11}$  for  
 575 the hotfilm data manifests in lower values of observed values of  $D_{11}$  when  
 576 compared to the model. Second-order structure functions exacerbate the sonic  
 577 anemometer’s poor performance, because the sonic cannot sample the smallest  
 578 scales in the flow and the structure function represents energy accumulated  
 579 from the smallest scales up to  $r$ . Note that it takes between one and two  
 580 decades of  $r/\eta$  for the structure functions obtained from the sonic to converge  
 581 to the hot-film values. Another noteworthy aspect of the structure functions  
 582 for the present value of  $Re_\lambda$  is that both data (our hot-film data as well as those  
 583 from Saddoughi and Veeravalli (1994)) and model differ from the prediction

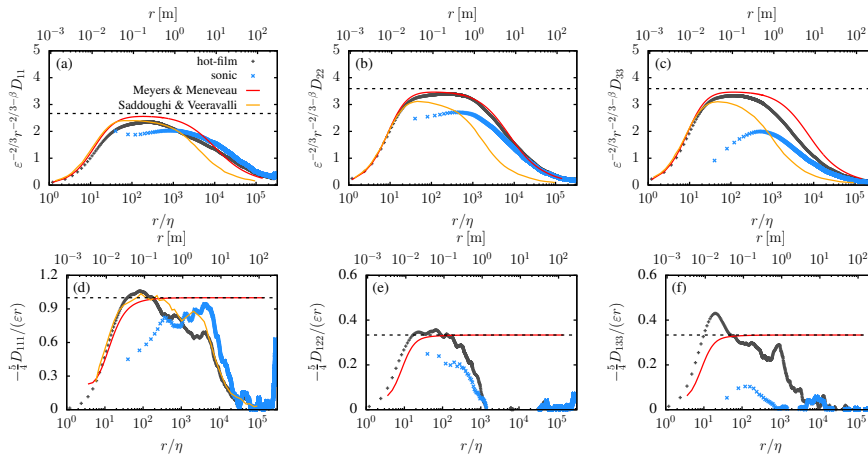


**Fig. 9** Nondimensionalized second- (upper panels) and third- (lower panels) order structure functions ((a,d) streamwise, (b,e) spanwise, (c,f) vertical). Hot-film/sonic anemometers data as grey/blue crosses, in addition to Meyers and Meneveau (2008)’s model and Saddoughi and Veeravalli (1994)’s data in red/yellow lines. The dashed black horizontal lines correspond to the theoretically predicted values for inertial range.

584 for the inertial range (dashed lines) obtained from the integral of the spectra  
 585 assuming an infinitely long Kolmogorov inertial range. The similarity between  
 586 the model and wind tunnel data indicates that this issue is not related to  
 587 canopy or stratification effects, rather this issue is most likely another effect  
 588 of the spectral bump in these measurements with limited Reynolds number.  
 589 Section 4.3 investigates this issue in more details.

590 The third-order structure function (Fig. 9 lower panels) is more difficult to  
 591 accurately calculate, as it requires longer time averaging to converge compared  
 592 to the second-order counterpart (Kaimal and Finnigan 1994; Podesta et al.  
 593 2009). Note that model estimates for all three third-order structure functions  
 594 are based on  $D_{11}$  only (in Eq. 12,  $D_{22}$  and  $D_{33}$  are never used), and the over-  
 595 prediction of the growth of  $D_{11}$  with  $r$  in the dissipation range (see Fig. 9(a))  
 596 compromises the agreement between model and data for the third order structure  
 597 functions. It is difficult to determine whether hot-film data is impacted  
 598 by the small sample size for  $(r/\eta) > 10^2$ . Clearly the sonic data is not able to  
 599 provide reliable values of the third-order structure function for this dataset,  
 600 probably due to the sensor’s path-averaging and flow distortion errors. Note  
 601 that the second-order structure function from the sonic starts deviating from  
 602 the hot-film around  $r/\eta \sim 10^{-4}$ , and that the third order structure function  
 603 is likely much more sensitive to small flow distortions than the second-order  
 604 counterparts.

605 The isotropy ratios of the second-order structure functions (Fig. 10) are  
 606 also impacted by the anisotropy in the spectral bump. The only ratio that is  
 607 not impacted much is  $D_{33}/D_{22}$ , which is in agreement with predictions from  
 608 local isotropy for more than half a decade of scales. It is very interesting that

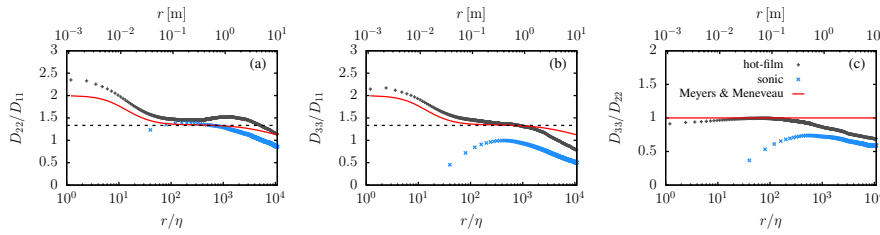


**Fig. 10** Ratios of the second-order structure functions. Hot-film (grey) and sonic (blue) anemometers data, in addition to Meyers and Meneveau (2008)'s model (red lines). The dashed black horizontal lines correspond to the theoretically predicted values for the inertial range.

609 the sonic data conforms reasonably well to the isotropy ratio of  $D_{22}/D_{11}$ ,  
 610 despite producing values of the second-order structure functions much lower  
 611 than those from the hot-film.

#### 612 4.3 Reynolds number dependence of the inertial range

613 The theoretical behavior of the inertial range when  $Re_\lambda \rightarrow \infty$ , as defined by  
 614 Kolmogorov's law, is commonly used as an indirect estimate of the dissipation  
 615 rate when only sonic data are available. Because results from the present anal-  
 616 yses raise concerns regarding the length and magnitude of the inertial range,  
 617 in particular of the structure function, it is important to investigate the impact  
 618 of the finite  $Re_\lambda$  on the inertial range for realistic atmospheric turbulence  
 619 conditions.

620 For large enough  $Re_\lambda$ , the behavior of the energy spectrum in the inertial  
 621 range should follow  $C_k L^{-\beta} \varepsilon^{2/3} \kappa^{-p}$ ,  $p = 5/3 + \beta$  (from Eq. (6)), as the func-  
 622 tions  $f_L$  and  $f_\eta$  should be approximately one. For the one-dimensional spec-  
 623 tra  $E_{\alpha\alpha}$ , this will correspond to a similar behavior  $C_\alpha L^{-\beta} \varepsilon^{2/3} \kappa^{-p}$ , in which  
 624  $C_1 = C_k / (0.5p(2+p))$  and  $C_2 = 0.5(1+p)C_1$  (Pope 2000, p. 228). Without  
 625 intermittency,  $\beta = 0$ ,  $p = -5/3$  and the usual  $C_1 = 18C_k/55$  and  $C_2 = 4C_1/3$   
 626 are obtained. If intermittency is considered, the value of  $p = -5/3 - \beta$  should  
 627 be taken into account, which corresponds to  $C_1 = 2592C_k/8113$  and  $C_2 =$   
 628  $97C_1/72$ . Although these intermittency corrections are small (since  $\beta = 1/36$ ),  
 629 they are not negligible, as it will be shown next.

630 For the second-order structure functions, the inertial range behavior cor-  
 631 responds to  $D_{\gamma\gamma} = C_\gamma^* L^{-\beta} \varepsilon^{2/3} r^q$  (from Eq. (11)), with  $q = p - 1$  and  $C_1/C_1^* =$   
 632  $\Gamma(1+q) \sin(\pi q/2) / \pi$  (Pope 2000, p. 701). Without intermittency,  $\beta = 0$ ,  
 633  $q = 2/3$ ,  $C_1^* \approx 4C_1$  and  $C_2^* = 4C_1^*/3$ . With intermittency,  $q = 2/3 + \beta$ ,  
 634  $C_1^* \approx 3.9C_1$  and  $C_2^* = 97C_1^*/72$ , a less negligible correction since  $q$  is closer to  
 635  $\beta$  compared to  $p$ .

636 In order to investigate the effect of  $Re_\lambda$  on the inertial range behavior, we  
 637 use the Meyers and Meneveau (2008)'s model combined with the atmospheric  
 638 data from Tsuji (2004). The field data and corresponding model's parameters  
 639 are provided in Tab. 2. Because the value of  $S_3$  was not provided with the

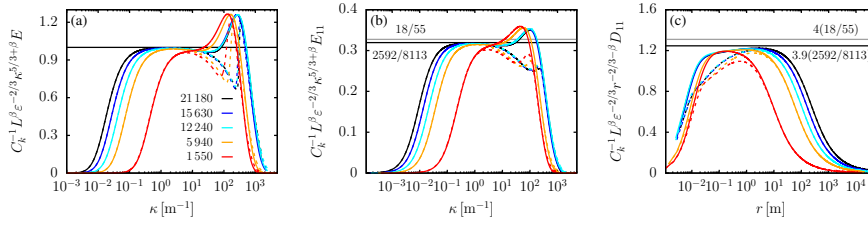
published data, and since there is no clear consensus regarding the behavior of  $S_3(Re_\lambda)$  (Sreenivasan and Antonia 1997) especially for atmospheric data (Djenidi et al. 2017), we chose to adjust the model used by Meyers and Meneveau (2008), namely  $S_3 = C_3 Re_\lambda^{9\mu/16}$  to the value  $S_3(Re_\lambda = 1550) = -0.41$  obtained here as an upper bound, and  $S_3(Re_\lambda = 17060) = -0.86$  obtained by Meyers and Meneveau (2008) for Tsuji (2004) data as a lower bound, as described in Tab. 2. These two curves approximately form an envelope around the  $S_3(Re_\lambda)$  data presented by Sreenivasan and Antonia (1997) (Fig. 5) for  $Re_\lambda \gtrsim 500$ .

Figure 11 shows the model predictions, assuming a 2 h time series with 2 kHz measurement frequency (to improve conversion of both large and small scales). For 3D spectra, it is possible to observe the extent of the impact of the value of  $S_3$ , which starts at  $\kappa \approx 20 \text{ m}^{-1}$ . According to this model, the inertial range extends at most one decade for the highest  $Re_\lambda$  evaluated here, regardless of the value of  $S_3$  used. In the upper limit of  $S_3$ , the deviation in the inertial range caused by the bump is less pronounced (and possibly masked in log-log plots), but still present. For  $Re_\lambda = 5940$  the inertial range plateau is already impacted by the production/dissipation ranges of the spectrum, not reaching the  $C_k$  value imposed. For the present data ( $Re_\lambda = 1550$ ) Meyers and Meneveau's (2008) model suggests that the inertial range is most likely absent, as discussed previously.

A similar inertial region exists for the one-dimensional spectrum (Fig. 11b), and the impact of the intermittency correction on the constant can be seen as small but non-negligible. Finally, the second-order structure function (Fig. 11c) does not reach the theoretically predicted values for the inertial range even for  $Re_\lambda = 21180$  (despite the constant being significantly reduced by the intermittency correction). Although the limitation is caused by the length of the inertial range, it is possible to see that it is particularly penalized by the large-scale range (since the small scales are very similar for the largest three  $Re_\lambda$  cases). The difference to the structure function prediction can be considered small for high-Reynolds number flows, but the lack of a clear inertial range in the structure function is remarkable. Furthermore, for  $Re_\lambda$  smaller than  $\sim 5000$ , as in the present data, this difference can be significant and it needs to be taken into account. Overall, this analysis indicates that finite Reynolds number effects on spectra and structure functions could be more ubiquitous in atmospheric flows than commonly assumed.

## 5 Conclusions

In this study we test an *in situ* calibration of hot-film data measured above a walnut orchard, using simultaneous sonic anemometer data. The method was developed based on the idea that the sonic data can be used as a replacement for the known velocity typically used in the calibration process. The method overcomes the need of constant recalibration of the sensor during the field experiment, relying only on properties of the sensors (yaw and pitch



**Fig. 11** Meyers and Meneveau (2008)’s model results for the atmospheric data including Tsuji’s (2004) data. (a) Three-dimensional spectrum, (b) streamwise 1D spectrum and (c) longitudinal second-order structure function, for  $Re_{\lambda} = 21\,180$  (black),  $15\,630$  (blue),  $12\,240$  (cyan),  $5\,940$  (orange) and  $1\,550$  (present data, red), using  $S_3 = C_3 Re_{\lambda}^{9\mu/16}$  and  $C_3 = -0.146$  (upper bound, solid) and  $-0.128$  (lower bound, dashed). Horizontal lines correspond to the theoretically predicted values for the inertial range without (grey) and with (black) intermittency.

683 parameters, geometry and relative position) and a physics-based relationship  
 684 (namely King’s law, as opposed to a numerical transfer function provided by  
 685 a neural network method). As a downside, we note that the present method  
 686 is very sensitive to small errors, as indicated by the effect of angle error on  
 687 isotropy ratios (Fig. 2), which would likely be automatically corrected by the  
 688 numerical transfer function in the neural network method. Because hot-film  
 689 anemometers require a consistent flow direction, which is particularly difficult  
 690 to achieve above a canopy due to strong turbulence intensities, it was not possible  
 691 to obtain long consecutive periods of data satisfying the quality-control  
 692 criteria. Nevertheless, it was possible to calibrate the hot-film using one long  
 693 3-hour period and to produce 33 2-min subblocks of hot-film data not contaminated  
 694 by data with higher wind direction angles, and yielding reasonably converged  
 695 statistics. The subblocks of data without error gaps provided by this  
 696 traditional calibration method is an upside compared to the neural network  
 697 method, whose effect of high turbulence intensity on small-scale statistics still  
 698 needs investigation.

699 To evaluate the quality of those statistics and validate the calibration  
 700 method, we compared the results with wind-tunnel data of Saddoughi and  
 701 Veeravalli (1994) (of similar  $Re_{\lambda}$ ), and with the model spectra of Meyers and  
 702 Meneveau (2008). The generally similar spectrum and structure function results  
 703 provide some confidence on the calibration technique, as most of the  
 704 discrepancies can be attributed to flow condition differences and on having  
 705 assumed isotropy.

706 Our data set suggests that the spectral bump in the energy spectrum is  
 707 anisotropic, with the streamwise component having less energy than the other  
 708 two components. It is entirely possible that this difference arises due to distortions  
 709 caused by the use of Taylor’s hypothesis, the presence of the canopy or the  
 710 stable stratification, something that cannot be investigated with the present  
 711 data. The presence of the spectral bump and, in particular, its anisotropy,  
 712 have many consequences for isotropy in the inertial range, especially at low  
 713  $Re_{\lambda}$  investigated here. Only a limited region that can be identified as the iner-

714 tial range exists in the streamwise spectrum (in which the bump is very small  
715 or non-existent), while no clear inertial range exists for the other two velocity  
716 components. The scales that conform more closely to inertial range scaling  
717 are impacted by the bump and its anisotropy (this impacts both scalings and  
718 isotropy ratios). The effect of the bump is amplified in the second-order struc-  
719 ture function, and its anisotropy produces much larger deviations than it is  
720 the case in the spectra.

721 The comparison with the model spectra provides an important additional  
722 insight: the structure function, by definition, cannot reach the prediction of  
723 infinitely large inertial range unless the  $Re_\lambda$  is sufficiently high. This remark,  
724 already discussed by Sreenivasan and Dhruva (1998) for atmospheric flow and  
725 recently by Antonia et al. (2019) for different types of flows, should be taken  
726 into account when using the inertial range of the structure function for flow  
727 predictions, such as the indirect estimation of the dissipation rate. Hot-film  
728 anemometry data can provide a useful alternative in this regard.

729 Finally, one of the original goals of this study was to investigate the quality  
730 of the sonic anemometer data in the inertial range, especially as sonic data  
731 is often used for indirect estimation of the dissipation rate. However, due to  
732 the experimental setup with an  $85^\circ$  angle between the two sensors, the sonic  
733 anemometer measurements are outside the ideal range for the sensor and likely  
734 include more errors than for smaller angles. If the data presented here provides  
735 any indication of the performance of sonic anemometers in the inertial range,  
736 the results are quite discouraging, in particular for canopy flows. If the hot-  
737 film data are to be trusted, then the dissipation estimated from the streamwise  
738 spectrum by the sonic anemometer would be slightly lower than the true value.  
739 All other estimates would be far off. In particular, the second-order structure  
740 functions would produce a very large underestimation of the dissipation rate  
741 despite showing proper inertial range scaling. Furthermore, when close enough  
742 to the ground, the CSAT3 data has a damped inertial range in all second-  
743 order structure functions ( $D_{11}$ ,  $D_{22}$  and  $D_{33}$ ), which is more pronounced in  
744  $D_{33}$  leading to wrong isotropy ratios. This is a cause for concern, since scaling  
745 and isotropy are frequently used as measure of the reliability of the data. A  
746 more carefully designed field experiment is needed to address some of these  
747 questions, ideally including a pre-calibration of the hot-film probe to check all  
748 calibration parameters, and a method for reorientation of the sensors in the  
749 field (as already present in the combo probe by Goldshmid et al. (2022), for  
750 example).

751 **Acknowledgements** The authors thank Steve Oncley and Gary Granger of NCAR's Earth  
752 Observing Laboratory for fruitful discussions and their assistance in accessing the CHATS  
753 hot-film anemometry data, and the Cilker family for allowing the CHATS experiment to  
754 take place in their orchard. We thank the anonymous reviewers for important observations  
755 and suggestions.

## 756 **Declarations**

757 **This version of the article has been accepted for publication, after**  
758 **peer review but is not the Version of Record and does not reflect**  
759 **post-acceptance improvements, or any corrections. The Version of**  
760 **Record is available online at: [http://dx.doi.org/10.1007/s10546-023-](http://dx.doi.org/10.1007/s10546-023-00826-w)**  
761 **00826-w. Use of this Accepted Version is subject to the publisher's**  
762 **Accepted Manuscript terms of use [https://www.springernature.com](https://www.springernature.com/gp/open-research/policies/accepted-manuscript-terms)**  
763 **/gp/open-research/policies/accepted-manuscript-terms.**

764 Ethical Approval

765 Not applicable.

766 Competing interests

767 The authors have no conflict of interest, financial or otherwise.

768 Authors' contributions

769 E.G.P. participated in the data collection and preparation. L.S.F and M.C.  
770 performed the data analysis and wrote the first draft of the manuscript. All  
771 authors provided critical feedback and helped shape the research, analysis and  
772 manuscript.

773 Funding

774 L.S.F. was funded by the São Paulo Research Foundation (FAPESP, Brazil),  
775 Grants No. 2018/24284-1 and 2019/14371-7. This material is based upon work  
776 supported by the National Center for Atmospheric Research, which is a ma-  
777 jor facility sponsored by the National Science Foundation under Coopera-  
778 tive Agreement No. 1852977. E.G.P. acknowledges supplemental support from  
779 NCAR's Geophysical Turbulence Program.

780 Availability of data and materials

781 The datasets generated during and/or analysed during the current study are  
782 available from the corresponding author on reasonable request.

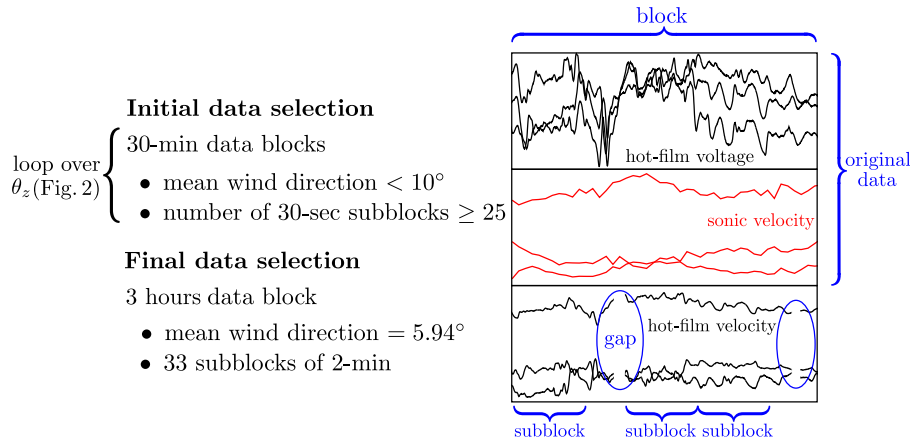


**Fig. 12** Summary of data selection and illustration of the blocks and subblocks used in this study. While the block consisted of a fixed period in the original data (hotfilm voltage and sonic velocity, 30-min and 3-hours long), the subblocks were formed in the final hot-film velocity series by selecting consecutive periods without gaps.

## 783 Appendix: Illustration of the calibration procedure and additional 784 statistics

785 The data processing required two steps, an initial data selection and a final  
786 data selection. The initial data selection consisted of going through all available  
787 data, and selecting the 30-min blocks that passed two quality criteria: mean  
788 wind direction relative to the hot-film's orientation smaller than  $10^\circ$  and a final  
789 number of 30-sec subblocks of at least 25. This stage was repeated correcting  
790 for angles  $80^\circ \leq \theta_z \leq 90^\circ$ , when the value of  $\theta_z = 85^\circ$  was selected.

791 The final data selection consisted of a single 3-hour block, from which 33  
792 subblocks of 2-min data without gaps were identified. These data were selected  
793 in order to increase the subblock length and the statistical convergence in  
794 the average between subblocks. It was also the only long period of several  
795 consecutive blocks that passed the initial data screening. See a summary in  
796 Fig. 12.

797 Figure 12 also illustrates the concept of blocks and subblocks. While the  
798 original data (hot-film voltage and sonic velocity) was separated in blocks (30-  
799 min and 3 hours long for the initial and final data selection, respectively), the  
800 final hot-film velocity presented gaps in the time series. Consecutive periods  
801 of data without gaps (30-sec and 2-min long for the initial and final data  
802 selection, respectively) were then selected as subblocks, which can start at the  
803 beginning of a block, immediately after a gap or after another subblock.

804 Figure 13 shows the mean and standard deviation of the three velocity  
805 components for each subblock, compared to the 3-hour value and comparing  
806 between sonic and hot-film values. Results show that the flow presented a  
807 slight increase in mean velocity and standard deviation over time, but it can be

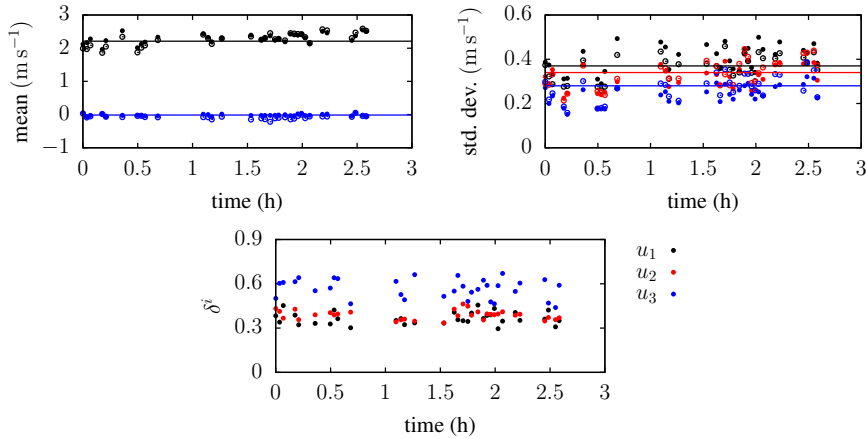


**Fig. 13** Block average (3 hours, solid lines) versus subblocks statistics (2-min, circles). Filled (open) circles are sonic (hot-film) data. Mean (top left), standard deviation (top right) and delta parameter (bottom) of the streamwise (black), spanwise (red) and vertical (blue) velocities.

808 considered approximately steady-state, justifying the average over subblocks  
 809 of all statistics presented in this study.

810 In order to compare sonic and velocity data directly, it is important to filter  
 811 both data at the frequencies in which they are comparable. As discussed in  
 812 Sec. 2.5, ideally, at most a 0.3 Hz cut-off frequency should be used (see Fig. 3).  
 813 However, a 2-min time series at 0.3 Hz of frequency has only 36 data points,  
 814 which are not statistically meaningful. Instead, we filtered the two datasets at  
 815 2 Hz, see Fig. 14. Notice that, at this frequency, the sonic data already diverges  
 816 from the hot-film data, which can be seen in Fig. 14. Furthermore, we estimated  
 817 the delta parameter as a quantitative measurement of the difference between  
 818 the two time series (Kit and Liberzon 2016; Goldshmid et al. 2022). The delta  
 819 parameter is defined as

$$\delta^i = \left\{ \frac{1}{N} \sum_{j=1}^N (\tilde{u}_{h,i}^{(j)} - \tilde{u}_{s,i}^{(j)})^2 \right\}^{1/2}, \quad (16)$$

820 where  $\tilde{u}_i^{(j)}$  is the  $j^{\text{th}}$  value of the velocity component  $i$  filtered at 2 Hz and  
 821 rescaled by their mean and standard deviation values of the subblock (sub-  
 822 scripts  $s$  and  $h$  are for sonic and hot-film, respectively). The values of  $\delta^i$  are  
 823 presented in Fig. 13, varying from 0.3 to 0.7. These values are relatively high  
 824 but of the same order of magnitude of the values obtained by Kit and Liberzon  
 825 (2016) and Goldshmid et al. (2022) using both traditional and neural network  
 826 calibration. We expect that in a more favorable setup, such as sonic pointing  
 827 to the streamwise direction, the sonic velocity would correspond to a better  
 828 “ground truth” for the velocity fluctuation and the  $\delta^i$  values would be lower.

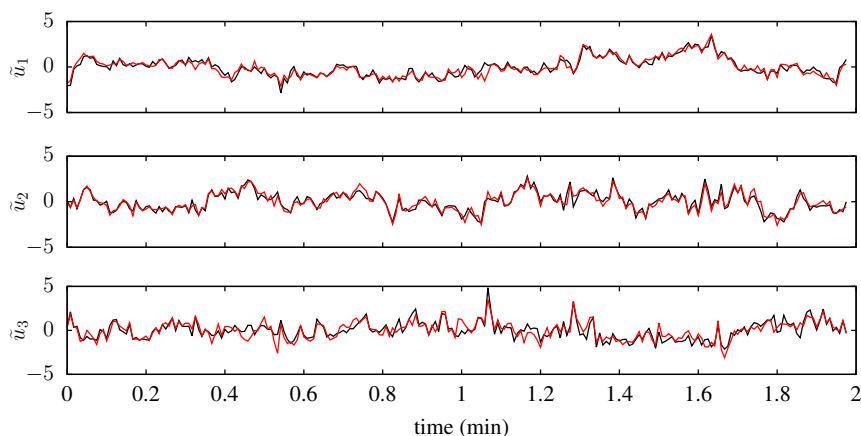


**Fig. 14** Time series of the filtered and rescaled velocity vector (filtered at the 2 Hz frequency, rescaled by their mean and standard deviation of the subblock) of the hot-film (black) and sonic (red) data, for the last 2-min block.

## References

- Amiro BD (1990) Drag coefficients and turbulence spectra within three boreal forest canopies. *Boundary-Layer Meteorology* 52(3):227–246
- Antonia RA, Tang SL, Djenidi L, Zhou Y (2019) Finite Reynolds number effect and the 4/5 law. *Phys Rev Fluids* 4:084,602, doi:10.1103/PhysRevFluids.4.084602
- Baldocchi DD, Meyers TP (1988) A spectral and lag-correlation analysis of turbulence in a deciduous forest canopy. *Boundary-Layer Meteorology* 45(1):31–58
- Cava D, Katul GG (2008) Spectral short-circuiting and wake production within the canopy trunk space of an alpine hardwood forest. *Boundary-Layer Meteorology* 126(3):415–431
- Djenidi L, Antonia RA, Talluru MK, Abe H (2017) Skewness and flatness factors of the longitudinal velocity derivative in wall-bounded flows. *Phys Rev Fluids* 2:064,608, doi:10.1103/PhysRevFluids.2.064608
- Dupont S, Patton EG (2012) Influence of stability and seasonal canopy changes on micrometeorology within and above an orchard canopy: The CHATS experiment. *Agricultural and Forest Meteorology* 157(0):11–29, doi:10.1016/j.agrformet.2012.01.011
- Dupont S, Patton EG (2022) On the influence of large-scale atmospheric motions on near-surface turbulence: Comparison between flows over low-roughness and tall vegetation canopies. *Boundary-Layer Meteorology* 184(2):195–230, doi:10.1007/s10546-022-00710-z
- Eaton JW, Bateman D, Hauberg S, Wehbring R (2020) GNU Octave version 5.2.0 manual: a high-level interactive language for numerical computations

- 854 Finnigan J (2000) Turbulence in plant canopies. *Annual Review of Fluid Me-*  
855 *chanics* 32(1):519–571, doi:10.1146/annurev.fluid.32.1.519
- 856 Frehlich R, Meillier Y, Jensen ML, Balsley B (2003) Turbulence mea-  
857 *surements with the cires tethered lifting system during cases-99: Cal-*  
858 *ibration and spectral analysis of temperature and velocity. Journal*  
859 *of the Atmospheric Sciences* 60(20):2487 – 2495, doi:10.1175/1520-
- 860 0469(2003)060<2487:TMWTCT>2.0.CO;2
- 861 Goldshmid RH, Winiarska E, Liberzon D (2022) Next generation combined  
862 *sonic-hotfilm anemometer: wind alignment and automated calibration pro-*  
863 *cedure using deep learning. Experiments in Fluids* 63(1):30–
- 864 Gulitski G, Kholmyansky M, Kinzelbach W, Lüthi B, Tsinober A, Yorish S  
865 (2007) Velocity and temperature derivatives in high-reynolds-number tur-  
866 *bulent flows in the atmospheric surface layer. Part 1. Facilities, meth-*  
867 *ods and some general results. Journal of Fluid Mechanics* 589:57–81,  
868 doi:10.1017/S0022112007007495
- 869 Hasse L, Dunckel M (1980) *Hot Wire and Hot Film Anemometers*, Springer  
870 US, Boston, MA, pp 47–63. doi:10.1007/978-1-4615-9182-5\_3
- 871 Hill RJ (1997) Applicability of Kolmogorov’s and Monin’s equa-  
872 *tions of turbulence. Journal of Fluid Mechanics* 353:67–81,  
873 doi:10.1017/S0022112097007362
- 874 Horst TW, Oncley SP (2006) Corrections to inertial-range power spectra  
875 *measured by Csat3 and solent sonic anemometers,1. path-averaging errors.*  
876 *Boundary-Layer Meteorology* 119(2):375–395, doi:10.1007/s10546-005-9015-
- 877 7
- 878 Horst TW, Semmer SR, Maclean G (2015) Correction of a non-orthogonal,  
879 *three-component sonic anemometer for flow distortion by transducer shad-*  
880 *owing. Boundary-Layer Meteorology* 155(3):371–395, doi:10.1007/s10546-
- 881 015-0010-3
- 882 Jørgensen FE (2005) How to measure turbulence with hot-wire anemometers  
883 – a practical guide. Dantec Dynamics, Tech rep
- 884 Kaimal JC, Finnigan JJ (1994) *Atmospheric boundary layer flows: their struc-*  
885 *ture and measurement.* Oxford University Press
- 886 Kelly M, Wyngaard JC (2006) Two-dimensional spectra in the atmospheric  
887 *boundary layer. Journal of the Atmospheric Sciences* 63(11):3066 – 3070,  
888 doi:10.1175/JAS3769.1
- 889 Kit E, Liberzon D (2016) 3d-calibration of three- and four-sensor hot-film  
890 *probes based on collocated sonic using neural networks. Measurement Sci-*  
891 *ence and Technology* 27(9):095,901, doi:10.1088/0957-0233/27/9/095901
- 892 Kit E, Cherkassky A, Sant T, Fernando HJS (2010) In situ calibration of  
893 *hot-film probes using a collocated sonic anemometer: Implementation of a*  
894 *neural network. Journal of Atmospheric and Oceanic Technology* 27(1):23–
- 895 41, doi:10.1175/2009JTECHA1320.1
- 896 Kit E, Hocut CM, Liberzon D, Fernando HJS (2017) Fine-scale turbulent  
897 *bursts in stable atmospheric boundary layer in complex terrain. Journal of*  
898 *Fluid Mechanics* 833:745772, doi:10.1017/jfm.2017.717

- 899 Kit E, Barami E, Fernando HJS (2021) Structure functions in nocturnal  
900 atmospheric boundary layer turbulence. *Phys Rev Fluids* 6:084,605,  
901 doi:10.1103/PhysRevFluids.6.084605
- 902 Lekakis I (1996) Calibration and signal interpretation for single and multiple  
903 hot-wire/hot-film probes. *Measurement Science and Technology* 7(10):1313–  
904 1333, doi:10.1088/0957-0233/7/10/004
- 905 Lekakis IC, Adrian RJ, Jones BG (1989) Measurement of velocity vectors with  
906 orthogonal and non-orthogonal triple-sensor probes. *Experiments in Fluids*  
907 7(4):228–240, doi:10.1007/BF00198002
- 908 Maciejewski PK, Moffat RJ (1994) Interpreting orthogonal triple-wire  
909 data from very high turbulence flows. *J Fluids Eng* 116(3):463–468,  
910 doi:10.1115/1.2910299
- 911 Mammarella I, Dellwik E, Jensen NO (2008) Turbulence spectra, shear  
912 stress and turbulent kinetic energy budgets above two beech forest sites  
913 in denmark. *Tellus B: Chemical and Physical Meteorology* 60(2):179–187,  
914 doi:10.1111/j.1600-0889.2007.00326.x
- 915 Metzger M, McKeon B, Holmes H (2007) The near-neutral atmospheric sur-  
916 face layer: turbulence and non-stationarity. *Philosophical Transactions of*  
917 *the Royal Society A: Mathematical, Physical and Engineering Sciences*  
918 365(1852):859–876, doi:10.1098/rsta.2006.1946
- 919 Meyers J, Meneveau C (2008) A functional form for the energy spec-  
920 trum parametrizing bottleneck and intermittency effects. *Physics of Fluids*  
921 20(6):065,109, doi:10.1063/1.2936312
- 922 Miller D, Lin J, Wang Y, Thistle H (1989) A triple hot-film and wind  
923 octant combination probe for turbulent air flow measurements in and  
924 near plant canopies. *Agricultural and Forest Meteorology* 44(3):353–368,  
925 doi:10.1016/0168-1923(89)90028-2
- 926 Pan Y, Chamecki M (2016) A scaling law for the shear-production range of  
927 second-order structure functions. *Journal of Fluid Mechanics* 801:459–474,  
928 doi:10.1017/jfm.2016.427
- 929 Patton EG, Horst TW, Sullivan PP, Lenschow DH, Oncley SP, Brown WOJ,  
930 Burns SP, Guenther AB, Held A, Karl T, Mayor SD, Rizzo LV, Spuler  
931 SM, Sun J, Turnipseed AA, Allwine EJ, Edburg SL, Lamb BK, Avissar R,  
932 Calhoun RJ, Kleissl J, Massman WJ, Paw U KT, Weil JC (2011) The canopy  
933 horizontal array turbulence study. *Bulletin of the American Meteorological*  
934 *Society* 92(5):593–611, doi:10.1175/2010BAMS2614.1
- 935 Patton EG, Sullivan PP, Shaw RH, Finnigan JJ, Weil JC (2016) Atmospheric  
936 stability influences on coupled boundary layer and canopy turbulence. *Journal*  
937 *of the Atmospheric Sciences* 73(4):1621–1647, doi:10.1175/JAS-D-15-  
938 0068.1
- 939 Peña A, Dellwik E, Mann J (2019) A method to assess the accuracy of  
940 sonic anemometer measurements. *Atmospheric Measurement Techniques*  
941 12(1):237–252, doi:10.5194/amt-12-237-2019
- 942 Podesta JJ, Forman MA, Smith CW, Elton DC, Malécot Y, Gagne Y (2009)  
943 Accurate estimation of third-order moments from turbulence measurements.  
944 *Nonlinear Processes in Geophysics* 16(1):99–110, doi:10.5194/npg-16-99-

2009

- 945 Pope SB (2000) *Turbulent Flows*. Cambridge University Press
- 946 Saddoughi SG, Veeravalli SV (1994) Local isotropy in turbulent boundary  
947 layers at high Reynolds number. *Journal of Fluid Mechanics* 268:333–372,  
948 doi:10.1017/S0022112094001370
- 949 Shapkalijevski M, Moene AF, Ouwersloot HG, Patton EG, de Arellano JVG  
950 (2016) Influence of canopy seasonal changes on turbulence parameteriza-  
951 tion within the roughness sublayer over an orchard canopy. *Journal of Ap-  
952 plied Meteorology and Climatology* 55(6):1391–1407, doi:10.1175/JAMC-D-  
953 15-0205.1
- 954 Shaw RH, Silversides RH, Thurtell GW (1974) Some observations of turbu-  
955 lence and turbulent transport within and above plant canopies. *Boundary-  
956 Layer Meteorology* 5(4):429–449, doi:10.1007/BF00123490
- 957 Singha A, Sadr R (2013) In situ calibration of four-wire hot-wire probes for  
958 atmospheric measurement. *Experimental Thermal and Fluid Science* 44:82–  
959 89, doi:10.1016/j.expthermflusci.2012.05.016
- 960 Skelly BT, Miller DR, Meyer TH (2002) Triple-hot-film anemometer perfor-  
961 mance in cases-99 and a comparison with sonic anemometer measurements.  
962 *Boundary-Layer Meteorology* 105(2):275–304
- 963 Sreenivasan KR, Antonia RA (1997) The phenomenology of small-  
964 scale turbulence. *Annual Review of Fluid Mechanics* 29(1):435–472,  
965 doi:10.1146/annurev.fluid.29.1.435
- 966 Sreenivasan KR, Dhruva B (1998) Is there scaling in high-reynolds-number  
967 turbulence? *Progress of Theoretical Physics Supplement* 130:103–120,  
968 doi:10.1143/PTPS.130.103
- 969 Su HB, Schmid HP, Grimmond CSB, Vogel CS, Oliphant AJ (2004) Spectral  
970 characteristics and correction of long-term eddy-covariance measurements  
971 over two mixed hardwood forests in non-flat terrain. *Boundary-Layer Me-  
972 teorology* 110(2):213–253
- 973 Tsuji Y (2004) Intermittency effect on energy spectrum in high-Reynolds num-  
974 ber turbulence. *Physics of Fluids* 16(5):L43–L46, doi:10.1063/1.1689931
- 975 Wyngaard JC, Clifford SF (1977) Taylor’s hypothesis and high-frequency  
976 turbulence spectra. *Journal of Atmospheric Sciences* 34(6):922 – 929,  
977 doi:10.1175/1520-0469(1977)034<0922:THAHTS>2.0.CO;2
- 978